Chinese Chemical Letters 37 (2026) 111606

Contents lists available at ScienceDirect

Chinese Chemical Letters

journal homepage: www.elsevier.com/locate/cclet

Hierarchically stabilized Pt with layered double hydroxide to construct nanoalloy for highly efficient cancer therapy

Xin Cao[a,b,1], Shizhuo Xiao[b,1], Aichun Kang[c,1], Yu Wei[b], Xueting Yang[a,b], Dawei Li[d,*], Wendi Liu[a], Małgorzata Szczerska[e], Jun Lu[a,*], Shanyue Guan[b,*]

[a] Beijng University of Chemical Technology, Beijing 100190, China
[b] Key Laboratory of Photochemical Conversion and Optoelectronic Materials, Technical Institute of Physics and Chemistry, Chinese Academy of Sciences, Beijing 100190, China
[c] Civil Aviation General Hospital, Beijing 100125, China
[d] Senior Department of Orthopedics, The Fourth Medical Center of PLA General Hospital, Beijing 100091, China
[e] Faculty of Electronics, Telecommunication, and Informatics, Gdansk University of Technology, Gdańsk 80-233, Poland

ARTICLE INFO

Article history:
Received 31 May 2025
Revised 15 July 2025
Accepted 17 July 2025
Available online 18 July 2025

Keywords:
Alloy
Layered double hydroxides
Reactive oxygen species
Redox
Homeostasis

ABSTRACT

Achieving optimal reactive oxygen species (ROS) production requires carefully balancing these interactions to maximize therapeutic efficacy. Herein, we have successfully developed a nanosystem through defect substitution using CuCoFe-layered double hydroxides (LDHs) as a template, followed by Pt reduction on the layer, the resulting nanoalloy, denoted as CuPt alloy@LDHs, demonstrating remarkable ROS production activity. This superior ROS production was attributed to its low Gibbs free energy barrier for generating hydroxyl radical (·OH), as confirmed by both characterizations and density functional theory (DFT) calculations. Additionally, the nanoalloy exhibits good (NO_x)-like activity, effectively disrupting the intracellular NADH/NAD^+ cycling balance and enabling self-cycling of endogenous H_2O_2. This work highlights that CuPt alloy@LDHs can effectively disrupt the redox homeostasis in tumor regions, significantly improving therapeutic efficacy and overcoming the limitations of current nanoalloy catalytic therapies.

© 2026 Published by Elsevier B.V. on behalf of Chinese Chemical Society and Institute of Materia Medica, Chinese Academy of Medical Sciences.

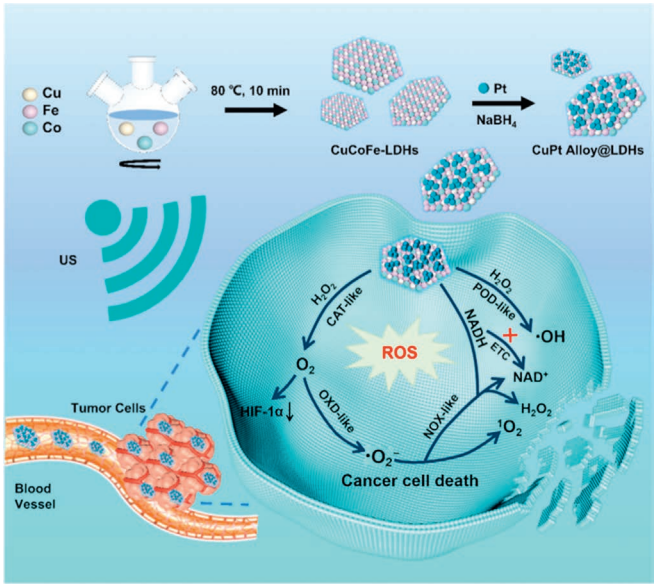
In contrast to normal cells, which primarily use mitochondrial oxidative phosphorylation for energy production, most cancer cells rely on aerobic glycolysis, a phenomenon known as the Warburg effect [1]. To disrupt this metabolic process, one effective strategy is to inhibit NADH, which plays a crucial role in glycolysis. Interestingly, NADH can react with superoxide radicals ($^{\bullet}O_2^-$) to regenerate NAD^+, providing an alternative approach [2,3]. The continuous generation of $^{\bullet}O_2^-$ is therefore essential for disrupting this pathway. Superoxide radicals, hydroxyl radicals, and other reactive ROS are critical for oxidative damage to cells [4,5]. Efficient regulation of these highly reactive free radicals requires high electron transfer capability and sufficient interaction sites to facilitate low activation energy and enhance catalytic efficacy [6,7].

Alloying is an innovative method for effectively regulating various free radicals. The optimized band structures in alloy materials provide abundant electronic orbitals, enhancing interactions with oxygen-containing molecules and improving energy transfer. Under this circumstance, it is superior than the chemotherapy, radiation therapy, with less side effect and specifically control the microenvironment. In this context, defect engineering techniques, such as vacancy and substitutional defects, play a crucial role [8–10]. These methods can organize and amplify active catalytic sites within nanosystems, thus mimicking the functions of natural enzymes. However, the independent operational characteristics of isolated defect sites and their cooperative mechanisms with biomolecules have not been fully explored. By incorporating both substitutional defects and oxygen vacancies (O_v) into a single nanostructure, highly efficient nanocatalysts can be developed, representing a groundbreaking strategy with the potential to significantly enhance anticancer efficacy [11,12].

Inspired by chemotherapeutic agents such as cisplatin, platinum is considered a promising candidate for cancer therapy. Platinum metal is renowned in the field of catalysis for its high catalytic activity, selectivity, and stability. Furthermore, platinum alloys often show significantly improved catalytic performance, enhanced durability, and optimized reaction selectivity through synergistic effects and modulation of the electric field properties [13,14]. These characteristics make platinum alloys a highly promising choice in catalysis, not only enhancing the efficiency of catalytic reactions but

* Corresponding authors.
E-mail addresses: ldw309@126.com (D. Li), lujun@mail.buct.edu.cn (J. Lu), guanshanyue@mail.ipc.ac.cn (S. Guan).
[1] These authors contributed equally to this work.

https://doi.org/10.1016/j.cclet.2025.111606
1001-8417/© 2026 Published by Elsevier B.V. on behalf of Chinese Chemical Society and Institute of Materia Medica, Chinese Academy of Medical Sciences.



Scheme 1. Schematic illustration of CuPt alloy@LDHs for US-enhanced catalysis for cancer therapy.

also offering new solutions for economic and environmental considerations in practical applications. Additionally, platinum helps capture electrons, while GSH tends to capture holes, thereby suppressing the recombination of electrons and holes. By applying this "alloying" design principle, LDHs with good elemental tunability and biocompatibility can be used as templates to create Pt alloy@LDH nanocatalysts [15–18]. These catalysts can feature abundant vacancies and platinum substitution, presenting a potential approach for effective catalytic applications.

Herein, we use CuCoFe-LDH as the precursor precisely prepare CuPt alloy@LDH. Cu can be regarded as the active center, enable both peroxidase (POD)-like and oxidase (OXD)-like activities. After the formation of nanoalloy, Pt can act to isolate Cu atom, and the electronic density of Cu is modulated by Pt, leading to enhanced enzymatic activity. This unique structure can generate a large amount of ROS in TME, attributed to the alloy structure and optimized Gibbs free energy barrier for producing ·OH, as verified by experiments and DFT calculations. This alloy structure design not only achieves unexpected catalytic effects but also provides a methodological basis for constructing of nanoalloy.

Preparation of CuPt alloy@LDHs: Weigh the CuCoFe-LDHs 0.3 g prepared by the above process, add 50 mL of DI water, and mechanically stir for about 30 min to make CuCoFe-LDHs evenly dispersed in the DI water. Add 0.05 g $H_2PtCl_6{\cdot}6H_2O$ and CuCoFe-LDHs solution and stir for 1 h to make $H_2PtCl_6{\cdot}6H_2O$ solution and CuCoFe-LDHs evenly mixed. $NaBH_4$:Pt^{4+} = 40:1, dissolve it in about 5 mL of DI water. Add two drops of KOH (2 mol/L) and make the $NaBH_4$ solution alkaline. Then, the $NaBH_4$ solution was added into the mixture, stirring and impregnating for 5 h under nitrogen protection. After the reaction, the prepared CuPt alloy@LDHs was centrifuged with a high-speed centrifuge, washed with DI water and ethanol for 3 times, and dried in a freeze-drying oven for 24 h.

Initially, CuCoFe-LDHs was prepared by a typical co-precipitation as a precursor. Subsequently, $H_2PtCl_6{\cdot}6H_2O$ was dripped into CuCoFe-LDHs, followed by the introduction of $NaBH_4$. Under the protection of N_2, Pt^{4+} can be partially reduced to Pt^0 and deposited on CuCoFe-LDHs to form CuPt alloy@LDHs (Scheme 1). The structure of both CuCoFe-LDH and CuPt alloy@LDHs were verified by X-ray diffraction (XRD) patterns. Both show obvious characteristic (00l) diffraction peaks centered at $2\theta = 5.82°$, 11.71° (Fig. 1A). Compared with CuCoFe-LDHs alone, the new merging peaks in a range from 40°−50° can be indexed to typical CuPt alloy peaks (PDF #48-1549), which can reveal the successful preparation of CuPt alloy@LDHs [19]. Its morphology was initially verified *via* transmission electron microscopy (TEM). The CuPt alloy@LDHs exhibits relatively uniform distribution with a diameter of about 120 ± 50 nm (Fig. 1B and Fig. S1 in Supporting information) while ultrasmall Pt nanoparticles were anchored on the CuPt alloy@LDHs. In addition, the longitudinal dimension of CuPt alloy@LDHs was further confirmed by atomic force micro-scope (AFM). The average thickness of CuPt alloy@LDHs were measured to be 4.5 ± 0.5 nm (Fig. S2 in Supporting information). Moreover, HRTEM showed that the crystal face spacing of the small size nanoparticle accumulation region is about 0.245 nm, which can be corresponded to the (200) plane of CuPt alloy@LDHs (Fig. 1C) [20]. After the introduction of Pt atoms, a twisted, unordered lattice can also be found, which lead to the occurrence of defects and thus improving the catalytic performance (Figs. 1D and E). The corresponding cross-sectional lines are illustrated in Fig. 1G. The STEM-EDS diagram shows the distribution of Pt, Cu, Co and Fe in CuPt alloy@LDH (Fig. 1F). The molar ratio of metal elements in the CuPt alloy@LDHs was determined by inductively coupled plasma atomic emission spectroscopy (ICP-AES), with the molar ratio of Cu/Co/Fe/Pt = 2.6:3.7:2.5:0.2. In addition, CuPt alloy@LDHs was well dispersed in PBS and DMEM for 7 days. There was no significant change in UV absorbance, indicating that CuPt alloy@LDHs had good stability in the physiological environment (Fig. S3 in Supporting information). The zeta potential of CuPt alloy@LDHs is determined to be +25.4 mV, which is significantly higher than that of CoCuFe-LDH (+18.3 mV), indicating the successful loading of Pt (Fig. S4 in Supporting information), and showed good water stability [21].

The surface chemistry and compositions variation on the transformation of CuCoFe-LDH to CuPt alloy@LDHs were identified by X-ray photoelectron spectroscopy (XPS). XPS survey spectra revealed that both CuCoFe-LDH and CuPt alloy@LDHs samples contained Cu, Co, Fe and C in their near-surface region, while Pt can only be found in CuPt alloy@LDHs (Fig. S5 in Supporting information). The high-resolution Pt 4f XPS spectrum for CuPt alloy@LDHs show the coexistence of Pt^0 and Pt^{2+}. The two characteristic peaks of 74.3 and 70.9 eV are assigned to $4f_{5/2}$ and $4f_{7/2}$ of Pt^0, while peaks at 75.8 and 71.5 eV are assigned to $4f_{5/2}$ and $4f_{7/2}$ of Pt^{2+}. The results showed that Pt^{4+}can be successfully reduced [22,23]. We further loaded the Pt cluster on the CuCoFe-LDHs as the comparison. Compared with CuCoFe/Pt, the binding energy of Pt $4f_{5/2}$ and Pt $4f_{7/2}$ in CuPt alloy@LDHs undergoes a red shift of 0.2 eV. This effect indicates that the electrons are transferred from Cu to Pt and therefore the electron density around Pt increases (Fig. 1H), The enhanced electron density of Pt can which is also beneficial for providing the electron for H_2O_2 decomposition, leading to the great potential for the generation of ROS. Fig. 1I shows the high-resolution XPS spectra of Cu for CuCoFe-LDHs and CuPt alloy@LDHs. In CuCoFe-LDHs, the peaks at 934.4 and 954.5 eV are $2p_{3/2}$ and $2p_{1/2}$ signals of Cu^{2+}. However, after forming CuPt alloy@LDHs, we found that Cu^0 peak appeared at 932.3 eV and 952.2 eV. At the same time, weak Cu^{2+} signals (934.4 and 954.5 eV) exist, and the Cu^0/Cu^{2+} peak-area ratio is about 3:7. There is no new valence state of Co and Fe after the reaction. Therefore, we conclude that in the presence of $NaBH_4$, the Cu^{2+} in CuCoFe-LDHs is reduced to a low-valence state (Cu^0), which is free from the bondage of LDH layer and interacts with Pt^0 due to electronegativity, thus forming CuPt alloy [24,25].

Afterwards, we further investigated the multienzyme-mimicking properties of CuPt alloy@LDHs. To verify if this alloy can ease the hypoxia condition in the tumor microenvironment (TME), we explored the catalase (CAT)-like catalytic activity (generation of oxygen) of CuPt alloy@LDHs. In the presence of H_2O_2,

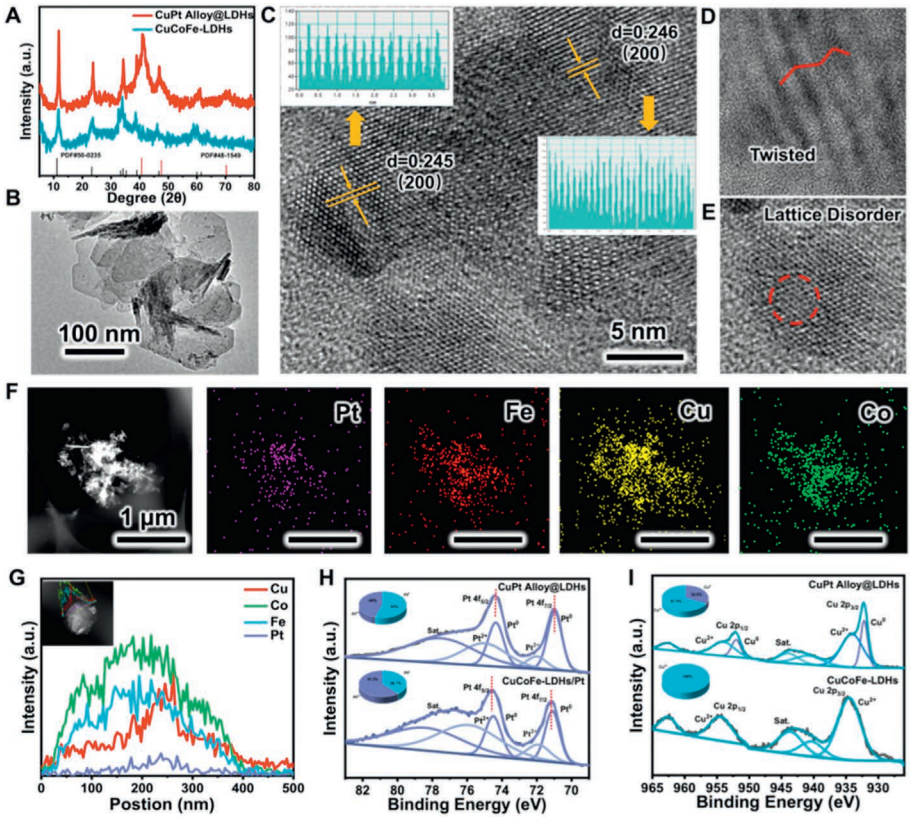


Fig. 1. Fabrication illustration and structure, morphology of CuPt alloy@LDHs. (A) XRD pattern of CuPt alloy@LDHs and CuCoFe-LDHs, respectively. (B) TEM images of CuPt alloy@LDHs. (C) The lattice fringe of CuPt alloy@LDHs. (D) Lattice disorder of CuPt alloy@LDHs. (E) Lattice distortion of CuPt alloy@LDHs. (F) The corresponding elemental mapping image of CuPt alloy@LDHs. (G) HAADF-STEM images of CuPt alloy@LDHs and EDS line scan. (H) Pt 4f XPS spectra of CuPt alloy@LDHs and CuCoFe-LDHs/Pt. (I) Cu 2p XPS spectra of CuPt alloy@LDHs and CuCoFe-LDHs.

the oxygen (O_2) production of CuPt alloy@LDHs is higher than that of CuCoFe-LDHs, indicating that CuPt alloy@LDHs has good CAT-like activity. In addition, activity values were determined by CAT enzyme kit [26]. The results show that the catalytic activity of CuPt alloy@LDHs nanozyme (4.506 U/mg) is nearly 5 times higher than that of CuCoFe-LDHs (0.9134 U/mg). Therefore, CuPt alloy@LDHs can effectively generate O_2 and further improve the hypoxia condition of TME (Fig. 2A).

In order to determine whether CuPt alloy@LDHs can produce reactive ROS, a probe of 3,3,5,5-tetramethylbenzidine (TMB) was utilized to study the generation of ROS from CuPt alloy@LDHs. The detection mechanism mainly relied on the reaction of the colorless TMB with ROS to form blue oxTMB products, and the corresponding characteristic absorption would enhance at the wavelengths of 652 nm (oxTMB) (Fig. 2B) [27]. In the presence of H_2O_2 (TME), the absorption peaks of CuPt alloy@LDHs and CuCoFe-LDHs both increased significantly as the time increased from 2 min to 10 min, which could verify the formation of ROS. Compared with CuCoFe-LDHs, CuPt alloy@LDHs has better ROS generation property and the absorbance intensity was obviously enhanced with the increasing concentration of CuPt alloy@LDHs (Fig. S6 in Supporting information). Subsequently, the electron spin resonance (ESR) was used to verify the above conclusion. The peak characteristics of 1:2:2:1 further confirmed that CuPt alloy@LDH can generate $^{\bullet}OH$. Meanwhile, the signal peak was further boosted under the action of US irradiation, which is consistent with the above results (Fig. 2F).

Additionally, the O_2 can further transfer into singlet oxygen ($^1O_2$) *via* a cascade reaction. In order to determine whether CuPt alloy@LDHs could produce $^1O_2$, 1,3-diphenylisobenzofuran (DPBF) was utilized to monitor the $^1O_2$ generation. We found that the characteristic peak at 410 nm decreased significantly over time, while the UV–vis absorption peak in the control group decreased slightly, indicating that CuPt alloy@LDHs could produce $^1O_2$ (Fig. 2D and Fig. S7 in Supporting information) [28]. ESR test was further performed to quantitatively measure the $^1O_2$ generation during the above process. As shown in Fig. 2E, $^1O_2$ could be generated during the OXD-like catalytic process of CuPt alloy@LDHs. Subsequently, the specific radical of $^{\bullet}OH$ was further identified by methylene blue (MB) degradation method. It is worth noting that the degradation ratio of CuCoFe-LDHs (27.5 %) and CuPt alloy@LDHs (43.9 %) under the same circumstance. This indicates that CuPt alloy@LDHs has a high POD-like activity, while the absorption peaks of MB+H_2O_2 do not decrease (Fig. 2C and Fig. S8 in Supporting information). In addition, after forming an alloy with Cu element, the electron transfer between Cu and Pt leads to the formation of electron-rich states around Pt, which further promoting the POD-like activity.

Encouraged by the multi-enzyme catalytic properties of CuPt alloy@LDHs, we further investigated whether CuPt alloy@LDHs has NO_X-like catalytic properties. The progress of NADH oxidation was monitored using UV–vis absorption spectroscopy. As shown in Fig. 2I, with the prolongation of the reaction time after the addition of CuPt alloy@LDHs, the characteristic absorption peak of NADH at 340 nm decreased significantly, while the absorption peak of NAD^+ at 260 nm gradually increased [29]. This change in the absorption spectrum is closely related to the conversion of NADH to NAD^+, suggesting that CuPt alloy@LDHs can induce the oxidation of NADH through NO_X-like activity. As an abundant endogenous antioxidant, GSH maintains the intracellular redox homeostasis and prevents ROS-induced cell damage. Therefore, consumption of GSH is an effective strategy for improving cancer therapy. Then, the catalytic ability of CuPt alloy@LDHs to deplete GSH was investigated using

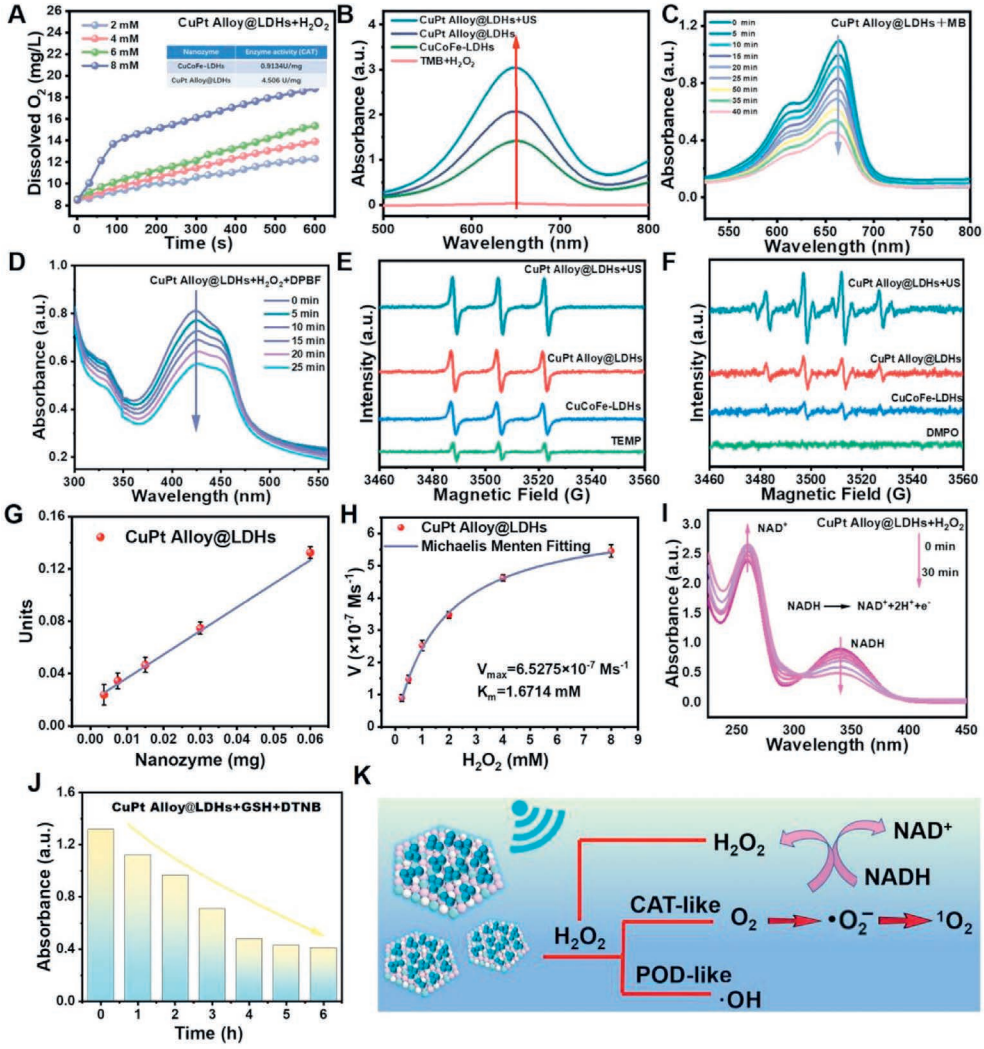


Fig. 2. (A) O_2 generation from H_2O_2 decomposition by CuPt alloy@LDHs (50 μg/mL). (B) TMB oxidation by ·OH from CuCoFe-LDHs, CuPt alloy@LDHs and CuPt alloy@LDHs+US in the presence of H_2O_2. (C) The POD-like activity of CuPt alloy@LDHs is indicated by UV–vis absorbance change trend of MB solution. (D) UV–vis absorbance of DPBF with various samples. (E) $^1O_2$ generation detected by ESR spectra. (F) ·OH generation detected by ESR spectra. (G) The specific nanozyme activity of CuPt alloy@LDHs. (H) Michaelis–Menten curve of CuPt alloy@LDHs. (I) Time-dependent absorption of NADH during 30 min of catalysis reaction by CuPt alloy@LDHs. (J) Time-dependent GSH depletion by CuPt alloy@LDHs. (K) The mechanism scheme of CuPt alloy@LDHs.

the 5,5-dithiobis-(2-nitrobenzoic acid) (DTNB) probe, whose color changed from colorless to yellow [30]. After being incubated with the CuPt alloy@LDHs, the concentration of GSH sharply decreased with longer incubation time (Fig. 2J and Fig. S9 in Supporting information), further revealing the GSH depleting catalytic activity of the CuPt alloy@LDHs. The mechanism scheme was illustrated in Fig. 2K.

The POD-like activity of CuPt alloy@LDHs was further investigated in different ways, the absorption intensity of oxTMB generated with different concentrations of CuPt alloy@LDHs nanozyme was measured to quantitatively evaluate the enzyme activity values (U/mg). According to the reaction curve of CuPt alloy@LDHs nanozyme under different concentrations, the initial linear parts were fitted to obtain the slopes, and then the SA value was calculated by plotting the obtained slopes with the corresponding mass. As can be seen in Fig. 2G and Fig. S10 (Supporting information), the CuPt alloy@LDHs show relatively high catalytic activity (1.84 U/mg). Steady-state dynamic analysis was performed with H_2O_2 (0.25, 0.5, 1, 2, 4, and 8 mmol/L) at a fixed concentration of CuPt alloy@LDHs nanozyme (Fig. S11 in Supporting information). The Michaelis Menten diagram and Lineweaver-Burk diagram were used for kinetic characterization, and the K_m value and V_{max} of CuPt alloy@LDHs were 1.67 mmol/L and 6.53×10^{-7} mol L^{-1} s^{-1}, respectively (Fig. 2H). Under the same test conditions, the K_m value and V_{max} of CuCoFe-LDHs are 3.62 mmol/L and 2.07×10^{-7} mol L^{-1} s^{-1}, respectively (Fig. S12 in Supporting information). The above results indicate that CuPt alloy@LDHs has a higher affinity with the reaction substrate and a faster POD-like catalytic rate, which is higher than the majority nanozymes (Fig. S13 in Supporting information) [31]. Therefore, this alloy can significantly enhance the generation of ROS and holds great potential for the cancer therapy. To further explore the mechanism of alloy enhanced enzymatic reaction, charge transfer was studied by electrochemical impedance spectroscopy (EIS). The smaller the radius of EIS, the stronger the charge transfer ability. Obviously, compared with CuCoFe-LDHs, CuPt alloy@LDHs has a smaller radius of EIS, indicating that it has the best charge transfer and transport capacity, and electrons can be transferred to the active site of alloy reaction. It is obvious that the semicircle is smaller than the CuCoFe-LDHs alone. It should be noted that CuPt alloy@LDHs + US group has the smallest semicircle, which indicates that the electron transfer and transport process is enhanced by US. It is proved that US provides energy for electron

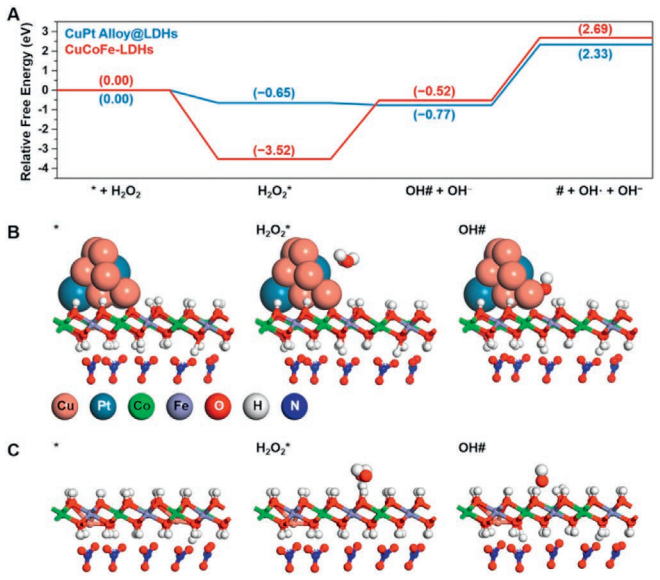


Fig. 3. (A) Gibbs free energy diagrams of H_2O_2 converted to ·OH over CuPt alloy@LDHs and CuCoFe-LDHs. (B) Optimized geometries of reaction intermediates for CuPt alloy@LDHs with a color code of elements. (C) Optimized geometries of reaction intermediates for CuCoFe-LDHs.

transfer, promotes electron accumulation on Pt, and improves catalytic performance (Fig. S14 in Supporting information).

As demonstrated above, the superior cancer therapy performance of CuPt alloy@LDHs compared to CuCoFe-LDHs derives from more facile generation of ROS, mainly ·OH. To reveal the intrinsic nature because ·OH is more facilely generated over CuPt alloy@LDHs than CuCoFe-LDHs, spin-polarized density functional theory (DFT) computations were performed to calculate the Gibbs free energy diagrams of H_2O_2 reduction to ·OH over CuPt alloy@LDHs and CuCoFe-LDHs, respectively (Fig. 3A). Detailed information of model construction and computational methods are described in Supporting information.

The reaction begins with the adsorption of H_2O_2. As shown in Figs. 3A and B, H_2O_2 is strongly adsorbed over both CuPt alloy@LDHs and CuCoFe-LDHs with the Gibbs free energy changes (ΔG) of −0.65 and −3.52 eV, respectively. The stronger adsorption of H_2O_2 over CuCoFe-LDHs derives from the hydrogen bonds between H_2O_2 and the hydroxyl group of CuCoFe-LDHs. After that, H_2O_2 is spontaneously splitted to ·OH and OH^- over CuPt alloy@LDHs with a ΔG of −0.12 eV while this step is difficult to happen over CuCoFe-LDHs because the ΔG is as high as 3.00 eV. The desorption of ·OH over CuPt alloy@LDHs needs to overcome an energy barrier of 3.10 eV [32]. The adsorption free energy of OH# over CuCoFe-LDHs (−3.21 eV) is also stronger than that over CuPt alloy@LDHs (−3.10 eV), resulting in a larger Gibbs free energy barrier for OH# desorption. The differences of adsorption free energies derive from their different reaction sites. For CuCoFe-LDHs, the reaction site is the surface hydroxyls while that for CuPt alloy@LDHs is CuPt alloy surface. For CuCoFe-LDHs, the hydrogen bonds between surface hydroxyls and the hydroxyls of reaction intermediates $H_2O_2^*$ and OH# are excessively strong, leading to its inferior catalytic performance. The calculated desorption free energy of ·OH is deduced to be overestimated than that in real reaction condition because the coverage of OH^* is much larger than the model in this work. By analyzing the Hirshfeld charges of CuPt alloy@LDHs, it is found that the Hirshfeld charge of Pt is −0.15 e, while those of Cu range from 0.03 e to 0.04 e, indicating that the electron of Cu transfers to Pt, which is also beneficial for providing the electron for H_2O_2 decomposition (Fig. 3C). In general, H_2O_2 can be well converted to ·OH over CuPt alloy@LDHs.

Considering that CuPt alloy@LDHs can produce a large number of ROS, simultaneously consuming GSH and disturb NADH/NAD^+ balance, leading to the disrupted homeostasis, further verified by cell experiments. We initially evaluated the cell uptake behavior of CuPt alloy@LDHs using confocal laser scanning microscope (CLSM) imaging. Hoechst stained (blue) HeLa cells and Cy5.5-labeled CuPt alloy@LDHs (red) were incubated for 1 h to 3 h. As shown in Fig. 4A, no red fluorescence signal was observed in control group. The CuPt alloy@LDHs treatment group began to show reddish fluorescence after 1 h, which mainly gathered in the cytoplasm. The red fluorescence gradually increased with the extension of time from 1 h to 3 h, indicating that CuPt alloy@LDH was internalized into cells through endocytosis [32]. The biocompatibility and biosafety were subsequently evaluated by CCK8 method. It should be noted that the cell viability of CuPt alloy@LDHs+H_2O_2+US group is significantly lower than that of CuPt alloy@LDHs+H_2O_2 and CuCoFe-LDHs+US groups (Fig. 4C and Fig. S15 in Supporting information), indicating that US can activate CuPt alloy@LDHs to produce a large number of ROS.

Additionally, a DCFH-DA probe was further used to measure the intracellular ROS concentration, and it could be found that green fluorescence is evident in the CuPt alloy@LDHs+H_2O_2+US group, indicating a large amount of intracellular ROS production, while no significant ROS-related fluorescence was observed in the control group (Fig. S16 in Supporting information). Apparently, CuPt alloy@LDHs+US can efficiently consume NADH in cancer cells by mimicking NO_X (Fig. 4D). The decrease of mitochondrial electron transfer chain (ETC) activity caused by NADH/NAD^+ imbalance can induce cell dysfunction [33]. Therefore, to further investigate the mechanism of CuPt alloy@LDHs-induced cellular damage, we used the JC-1 fluorescent probe to assess its effect on mitochondrial function. As shown in Fig. 4B, an obvious increase in green fluorescence intensity was observed in CuPt alloy@LDHs+H_2O_2+US treated cells, indicating significant depolarization, which may be due to severe mitochondrial respiratory chain disruption. Thus, CuPt alloy@LDHs+US could effectively cause mitochondrial dysfunction in tumor cells and accelerate oxidative stress in tumor cells, leading to cancer cell death. Subsequently, the fluorescent probe BODIPY 581/591 C11 was used to assess intracellular LPO levels. BODIPY 581/591 C11 readily binds to cell membranes and emits red fluorescence. When LPO accumulate in cells, BODIPY 581/591 C11 acts as a reducing agent, stimulating and emitting the spectrum to the shorter wavelengths of green fluorescence. Cell CLSM imaging showed that Control group, Control+US group and H_2O_2 group all showed red fluorescence, CuCoFe-LDHs+H_2O_2 group showed weak green fluorescence, CuPt alloy@LDHs+H_2O_2 green fluorescence was obvious, while the red fluorescence became weak. In the CuPt alloy@LDHs+H_2O_2+US group, strong green fluorescence was shown, and red fluorescence was further weakened, indicating large accumulation of LPO in the tumor, which can also indue ferroptosis (Fig. 4E).

Then we used the Si-DMA fluorescence probe to detect the $^1O_2$ level in the cell. When $^1O_2$ was present, internal peroxides would be generated in the anthracene site of Si-DMA, and the red fluorescence intensity of Si-DMA would be enhanced. In Fig. 4F, CuPt alloy@LDHs+H_2O_2 group has obvious red fluorescence. Under US irradiation, the red fluorescence was further enhanced, while there was no obvious red fluorescence in the control group, indicating that CuPt alloy@LDHs combined with US can produce $^1O_2$ in the tumor. In order to analyze the effect of intracellular oxygenation on alleviating hypoxia, we determined the intracellular O_2 level using a tris(4,7-diphenyl-1,10-phenanthroline) ruthenium(II) dichloride complex ($[Ru(dpp)_3]Cl_2$) oxygen probe. The red fluorescence of $[Ru(dpp)_3]^{2+}$ was significantly enhanced when the intracellular

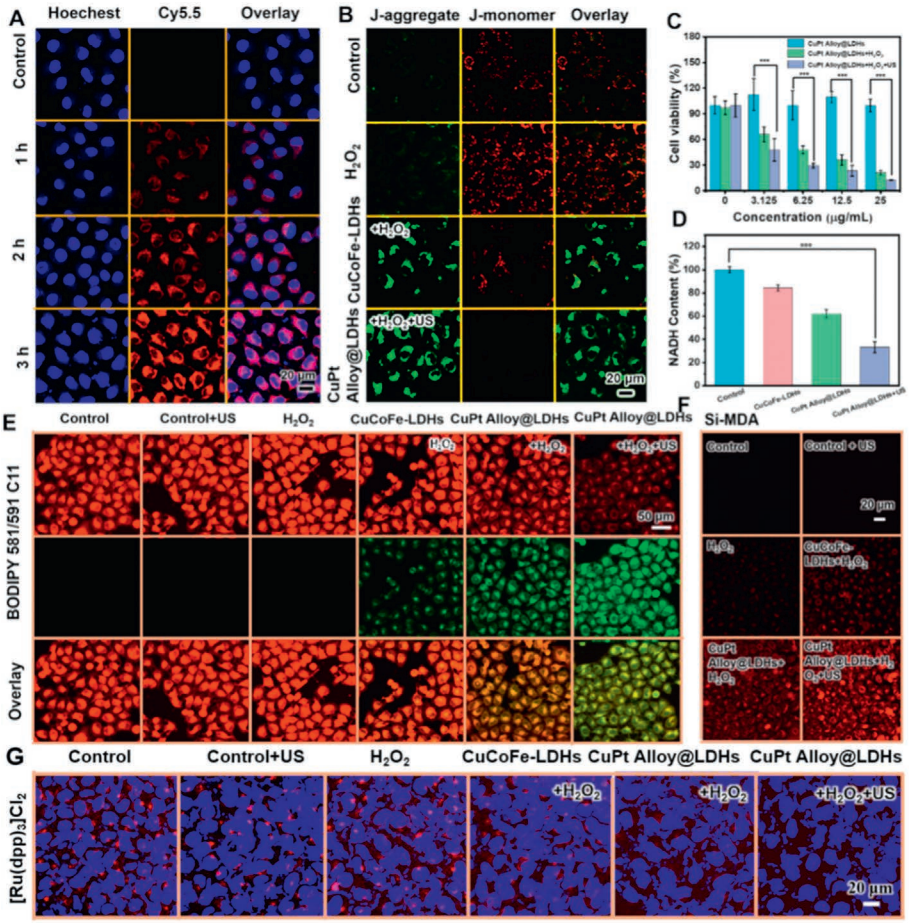


Fig. 4. (A) CLSM images of Cy5.5-label CuPt alloy@LDHs taken by HeLa cells. (B) JC-1 staining of HeLa cells in different groups. (C) Cell viability of HeLa cells incubated with CuPt alloy@LDHs with different treatments. $^{***}P < 0.001$. (D) NADH content of cancer cells in different treatment groups. (E) BODIPY 581/591 C11 containing HeLa cells after different treatments, green fluorescence corresponds to LPO accumulation. (F) The Si-MDA probe was used to detect $^1O_2$ in mitochondria. The strong red fluorescence indicated that a large amount of $^1O_2$ was produced. (G) CLSM images $[Ru(dpp)_3]Cl_2$ in HeLa cells after different treatments.

oxygen content is reduced, and has weak red fluorescence when the intracellular oxygen content is increased [34]. In Fig. 4G, the CuPt alloy@LDHs+H_2O_2+US group showed weak red fluorescence after US irradiation, which proved that the intracellular oxygen supply was effective. In addition, CLSM imaging on cells stained with both Calcein-AM (staining living cells with green fluorescence) and PI (staining dead cells with red fluorescence) were used to further test their anticancer properties. It was found that HeLa cells were almost completely killed in the CuPt alloy@LDHs+US group, and PI emitted a strong red fluorescence signal, indicating that CuPt alloy@LDHs+US effectively induced apoptosis (Fig. S17 in Supporting information). In order to further explore the mechanism of cell death, HeLa cells were co-incubated with ROS inhibitors, and the survival rate of cells was found to be over 90%, which proved that ROS is the main substance that destroys mitochondrial function and induces ferroptosis (Fig. S18 in Supporting information) [35]. These results suggest that CuPt alloy@LDHs has effective anticancer properties by producing highly toxic ROS through a cascade catalytic reaction that destroys mitochondrial function.

The interesting cascade catalytic anti-cancer properties of CuPt alloy@LDHs *in vitro* encourage us to investigate its anti-cancer efficacy *in vivo*. To observe the therapeutic effect of CuPt alloy@LDHs on BALB/c mice with HeLa tumor. To verify whether CuPt alloy@LDHs can be highly retained at tumor sites, we monitored its distribution *in vivo* by labeling CuPt alloy@LDHs with the near-infrared dye indolyl ring green (ICG). After injection, it accumulated at the tumor site with the increase of time, and the fluorescence intensity at the tumor site reached the maximum 6 h (Figs. 5A and B). Subsequently, the fluorescence intensity decreased gradually, indicating that CuPt alloy@LDHs has a good accumulation capacity at the tumor site and gradually metabolism *in vivo*.

Magnetic resonance imaging (MRI) is one of the most commonly used imaging methods in clinical diagnosis, which can overcome the obstacle of limited penetration depth of exogenous stimulation [36]. Therefore, the MR imaging capability of CuPt alloy@LDHs was studied due to the presence of paramagnetic components in CuPt alloy@LDHs. As revealed in Fig. S19 (Supporting information), both $1/\Delta T_1$ have a linear relationship with Fe concentration. The relaxation of the CuPt alloy@LDHs sample is 8.76 L $mmol^{-1}$ s^{-1} at $1/\Delta T_1$. CuPt alloy@LDHs has good contrast enhancement ability in magnetic resonance imaging (Fig. 5C).

Encouraged by the high catalytic performance of CuPt alloy@LDHs, we further investigated the therapeutic effect of CuPt alloy@LDHs nanozymes *in vivo*. BALB/c mice were divided into 5 groups ($n = 4$): (1) Control group; (2) Control+US; (3) CuCoFe-LDHs group; (4) CuPt alloy@LDHs group; (5) CuPt alloy@LDHs+US group. Compared with the Control group and the Control+US group, the tumor growth of CuPt alloy@LDHs group was significantly inhibited, indicating that CuPt alloy@LDHs has a good therapeutic effect. At the same time, CuPt alloy@LDHs combined with the US group showed almost complete inhibition of tumor growth, demonstrat-

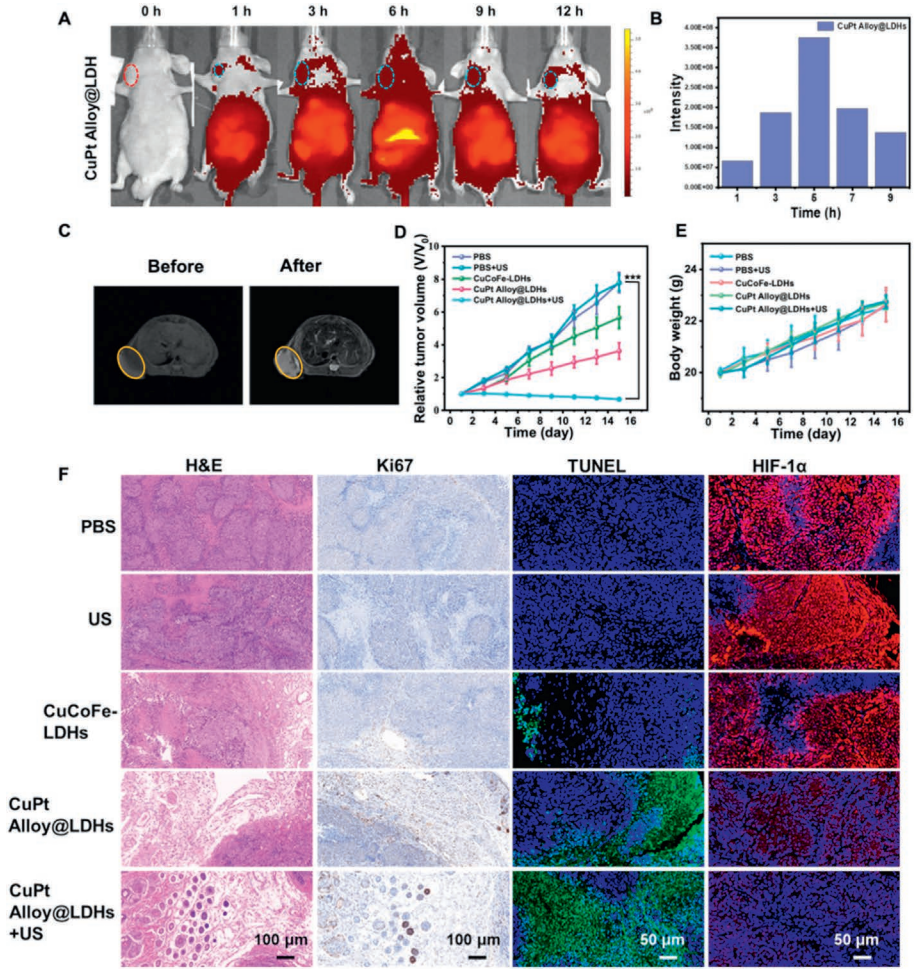


Fig. 5. (A) *In vivo* fluorescence images and (B) the corresponding fluorescence intensity of HeLa-tumor-bearing mice injected with ICG-CuPt alloy@LDHs at various time points. (C) The corresponding tumor volume change curves after treatment with different formulas ($n = 4$, mean ± *S*.D., $^{**}P < 0.01$ and $^{***}P < 0.001$). (D) Body weight curves after indicated treatments ($n = 4$). (E) *In vivo* T_1−MRI imaging of HeLa-bearing mice before and after injected with a CuPt alloy@LDHs. (F) H&E, TUNEL, Ki67 and HIF-1α tumor-stained tissue images of each treatment group.

ing the feasibility of our enhanced CuPt alloy@LDHs catalytic antitumor therapy (Fig. 5D and Fig. S20 in Supporting information). Within two weeks of treatment, there was no significant change in body weight in each group (Fig. 5E). ICP-AES analysis was performed to assess Cu element clearance kinetics in blood over time. The blood circulation half-time of CuPt alloy@LDHs in the bloodstream followed a classical two-compartment pharmacokinetic model with the terminal elimination half-lives of 0.17 h and 3.28 h for the central component and peripheral component, respectively (Fig. S21 in Supporting information).

In addition, hematoxylin and eosin (H&E) staining of tumor cells confirmed that CuPt alloy@LDHs caused more serious damage to tumor tissues. Meanwhile, dUTP-biotin nick and labelling (TUNEL) demonstrated positive apoptotic cells, while much fewer Ki67-positive proliferative cells in the tumor tissue for CuPt alloy@LDHs treatment than other formulations. Confocal fluorescence images, HIF-1α stained tumor sections confirmed that CuPt alloy@LDHs could reverse tumor hypoxia, and CuPt alloy@LDHs had good oxygen-producing properties in TME (Fig. 5F). In addition, biosafety was carried out for Control group, Control+US group, CuCoFe-LDHs group, CuPt alloy@LDHs and CuPt alloy@LDHs+US. H&E-stained mouse main organs were shown, and no obvious tissue inflammation was found after all kinds of processing, demonstrating good biocompatibility (heart, liver, spleen, lung and kidney) (Fig. S22 in Supporting information).

In summary, we have successfully developed CuPt alloy@LDHs nanocatalyst, which can effectively inhibit tumor growth by interfering with intracellular redox homeostasis. After exposure to TME, a large number of ROS can be produced at the tumor site through OXD-like and POD-like catalytic activity, causing oxidative damage to tumor cells. Most importantly, CuPt alloy@LDHs can also disrupt the NaDH/NAD^+ cycle, resulting in the decline of mitochondrial ETC activity, disrupting cell redox homeostasis, and thus significantly enhancing the efficacy of tumor therapy. At the same time, CuPt alloy@LDHs nanozyme can also be activated under US irradiation, further amplifying tumor oxidative stress. After the administration of CuPt alloy@LDHs in HeLa tumor mice models, ideal tumor suppression was achieved. This strategy of tumor therapy, which disrupts the redox homeostasis of tumor region by simulating cascade catalytic reaction, overcomes the shortcomings of current catalytic therapy and further broadens its application in the field of cancer therapy.

CRediT authorship contribution statement

Xin Cao: Resources, Project administration. **Shizhuo Xiao:** Data curation. **Aichun Kang:** Validation. **Yu Wei:** Writing – original draft. **Xueting Yang:** Visualization, Conceptualization. **Dawei Li:** Visualization, Supervision. **Wendi Liu:** Software. **Małgorzata Szczerska:** Supervision, Software. **Jun Lu:** Project administration,

Methodology. **Shanyue Guan:** Writing – review & editing, Funding acquisition.

Declaration of competing interest

The authors declare no conflict of interest.

Acknowledgments

This study was supported by Beijing Natural Science Foundation (No. 7244312). Youth Innovation Promotion Association of Chinese Academy of Sciences (No. 2019027). The National Natural Science Foundation of China (Nos. 21805293, 81972081) and Cross-Innovation Open Project of Food Flavor and Health, Beijing Technology & Business University (No. FFHCI-2025076). All animal experiments were performed in compliance with the relevant laws and institutional guidelines of the eighth medical center of PLA general hospital and approved by the Institutional Animal Care & Welfare Committee of the eighth medical center of PLA general hospital (License number: 30920220308112826).

Supplementary materials

Supplementary material associated with this article can be found, in the online version, at doi:10.1016/j.cclet.2025.111606.

References

[1] Y. Du, R. Zhang, J. Yang, et al., Adv. Funct. Mater. 32 (2022) 2111784.
[2] F. Du, L. Liu, Z. Wu, et al., Adv. Mater. 33 (2021) 2101095.
[3] Y. Xing, L. Wang, L. Wang, et al., Adv. Funct. Mater. 32 (2022) 2111171.
[4] S. Li, H. Ding, J. Chang, et al., Adv. Healthc. Mater. 12 (2023) 2300652.
[5] W. Hu, Y. Ma, Z. Zhan, et al., Cyborg Bionic Syst. 2022 (2022) 9763420.
[6] S. Wu, L. Xu, C. He, et al., Adv. Sci. 10 (2023) 2300686.
[7] H.S. Tuli, J. Kaur, K. Vashishth, et al., Arch. Toxicol. 97 (2023) 103–120.
[8] B. Wang, H. Zhang, J. An, et al., Nano Lett. 19 (2019) 3505–3518.
[9] B. Tian, R. Tian, S. Liu, et al., Adv. Mater. 35 (2023) 2304262.
[10] L. Yang, B. Tian, Y. Xie, et al., Adv. Mater. 35 (2023) 2300648.
[11] X. Wu, H. Yang, X. Chen, et al., Biomaterials 269 (2021) 120654.
[12] N. Li, Y. Gao, B. Li, et al., Nano Lett. 22 (2022) 5427–5433.
[13] J. Deng, S. Xu, W. Hu, et al., Biomaterials 154 (2018) 24–33.
[14] G. Li, S. Wang, D. Deng, et al., ACS Nano 14 (2020) 1586–1599.
[15] L. Zhuang, P. Wang, K. Song, et al., Chem. Eng. J. 497 (2024) 154500.
[16] M. Mo, Y. Jiang, A. Kang, et al., ACS Appl. Mater. Inter. 16 (2024) 23003–23014.
[17] Z. Wang, J. Liu, M. Feng, et al., Chem. Eng. J. 470 (2023) 144020.
[18] L. Wang, B. Zhang, X. Yang, et al., Bioact. Mater. 20 (2023) 126–136.
[19] Y. Dai, C. Xu, X. Sun, et al., Chem. Soc. Rev. 46 (2017) 3830–3852.
[20] Z. Dong, P. Liang, G. Guan, et al., Angew. Chem. Int. Ed. 61 (2022) e202206074.
[21] B. Yu, W. Wang, W. Sun, et al., J. Am. Chem. Soc. 143 (2021) 8855–8865.
[22] J. Xie, C. Liang, S. Luo, et al., ACS Appl. Mater. Inter. 13 (2021) 27934–27944.
[23] Y. Liu, B. Wang, J. Zhu, et al., Adv. Mater. 35 (2023) 2208512.
[24] E. Yuan, P. Ni, W. Zhuang, R. Jian, P. Jian, J. Catal. 382 (2020) 256–268.
[25] M. Chang, Z. Hou, M. Wang, et al., Angew. Chem. Int. Ed. 134 (2022) e202209245.
[26] L. Li, H. Liu, J. Bian, et al., Chem. Eng. J. 397 (2020) 125438.
[27] X. Liu, X. Wang, B. Yang, et al., Nano Res. 16 (2023) 4775–4785.
[28] M. Huo, L. Wang, Y. Wang, et al., ACS Nano 13 (2019) 2643–2653.
[29] T. Zhang, Z. Liu, W. Tang, et al., Nano Today 46 (2022) 101620.
[30] Y. Wang, D. Meng, X. Zhao, et al., Appl. Catal. B: Environ. 273 (2020) 119064.
[31] J. Zou, J. Zhu, Z. Yang, et al., Angew. Chem. Int. Ed. 59 (2020) 8833–8838.
[32] D. Wen, K. Li, R. Deng, et al., J. Am. Chem. Soc. 145 (2023) 3952–3960.
[33] B. Liu, S. Liang, Z. Wang, et al., Adv. Mater. 33 (2021) 2101223.
[34] S. Dong, Y. Dong, B. Liu, et al., Adv. Mater. 34 (2022) 2107054.
[35] S. Kim, T. Tachikawa, M. Fujitsuka, et al., J. Am. Chem. Soc. 136 (2014) 11707–11715.
[36] Z. Yang, J. Wen, Q. Wang, et al., ACS Appl. Mater. Inter. 11 (2018) 187–194.